

Large cluster formation in a simple model for globular colloidal aggregates

Antonio Díaz-Pozuelo¹ and Diego González-Salgado², and Enrique Lomba¹

¹*Instituto de Química Física Blas Cabrera, CSIC,
Calle Serrano 119, E-28006 Madrid, Spain*

²*Modelización y Simulación de Materiales Nanoestructurados,
Universidad de Vigo, Unidad Asociada al CSIC por el IQF,
Departamento de Física Aplicada, E-32004, Ourense, Spain*

Abstract

A simple model of fluid whose constituent particles interact via a short range attractive and long range repulsive potential is used to model the aggregation into large spherical-like clusters made up of hundreds of particles. The model can be thought of as a simplistic representation of membraneless organelles or a straightforward rendition of colloid flocculation into large spherical aggregates. We illustrate how temperature and particle density influence the cluster size distribution and affect inter- and intra-cluster dynamics. The system is shown to exhibit two well separated length and time scales, which can be tuned by the balance between repulsive and attractive forces. Interestingly, cluster aggregates at moderate/low temperatures approach cluster glassy phases whereas the clusters itself are liquid droplets. These states present a strong suppression of density fluctuations for a significant range of relatively large wavelengths, meeting the criterion of effective disordered hyperuniform materials.

I. INTRODUCTION

Spontaneous pattern formation and self-limiting association can be deemed a key phenomenon both in soft matter and biological physics[1]. In the former, colloidal suspensions are characteristic examples in which a variety of patterns have been identified in systems as disparate as amphiphilics[2], or proteins, such as lysozyme[3] or antibodies[4] (see Kovalchuk and coworkers[5] and references therein for a more comprehensive review of experimental examples). As a particularly interesting illustration of self-limiting aggregates, recently Sweatman and Lue [6] have argued that the formation of giant clusters due to the competition between attractive and repulsive interactions might well be behind the condensation of proteins/nucleic acids into membraneless organelles (MLOs) within the nuclei of eukaryotic cells [7]. This is an alternative view to the “traditional” liquid-liquid phase separation picture that is common among the structural biology community[8].

As to pattern formation in soft matter systems, there is a growing interest on this subject, in particular for the possibilities that non-templated thermodynamically controlled nano-patterning[9–11] offers in the field of nanotechnology. In this connection, simple models that exhibit short range attraction and long range repulsion (SALR), [12, 13] have shown to be able to reproduce the experimental behavior in great detail. In the pioneering work of Andelman and coworkers it was predicted by means of a mean field theory that, for a sufficiently large amplitude of repulsive interactions, modulated cluster phases will emerge[14]. The central role of attraction/repulsion competition in the build-up of globular (MLO-like) bubble cluster, and ordered modulated phases or bicontinuous percolating clusters that span up to macroscopic sizes, has been known for more than three decades[13]. The shape and size of the clusters and their spatial organization is directly determined by the balance between attractive and repulsive forces, as shown by the ground state calculations of Mossa et al.[15]. Obviously, thermodynamic conditions (density and temperature/pressure) play a key role as well. Recently Liu and Xi [16] proposed a classification of SALR potentials in terms of the ratio between repulsive and attractive forces and particle size. Thus SALR potential are classified into type-I (range of the attraction is less than 20% of the particle size, and range of the repulsion is a fraction of the particle size), type-II (range of the attraction less than 20% of the particle size, range of repulsion is comparable or larger than particle size) and type-III (range of attraction beyond 20% of particle size and range of repulsion as in type

II). In Ref. [16] it was shown that these three classes of interactions lead to specific features as to their phase behavior and cluster morphology.

The phase behavior of SALR systems has been dealt with extensively using theoretical [14, 17–21] and simulation approaches [22–24]. A more comprehensive summary of relevant contributions in this connection can be found in recent review works [16, 25, 26]. It should be stressed that in all these instances, the long range repulsive component of the interaction is essential for the self-limitation of the aggregation process, preempting condensation/demixing transitions. The latter would drive the system towards spatially separate macroscopic phases[24] instead of the microstructuring induced by clustering.

It is worth mentioning that other alternative approaches can explain self-limitation in aggregation processes as well. Such is the case, for instance, when the presence of specific interactions in mixtures limits the growth of the aggregate due the saturation of bonding sites by one of the components[27], in parallel with the chain termination in radical polymerization reactions.

Finally, as stated by Klix and coworkers [23] SALR systems are intrinsically frustrated, and this also affects their dynamics, which is mostly controlled either by mesoscopic order or by metastable disorder[23]. These authors actually identify three dynamically arrested phases in their SALR model with long range electrostatic repulsions: a Wigner glass (moderate packing fraction/weak attractive interactions), a cluster glassy state (low packing fraction, strong attractive interactions), and a percolating gel phase (high packing fraction/strong attractive interactions). The possibility of the existence of a Wigner glass phase in disordered systems with long range electrostatic interactions was first postulated by Bose and Wilke using mode coupling theory[28]. Dawson et al [29] further analyzed in detail the possibility of dynamically arrested states in colloids stemming from either attractive or repulsive forces, whose ratio, as Klix et al. [23] have shown, controls both the type of dynamics and topology of the glassy states. Experimental evidence of colloidal glassy states is extensive and, for instance, numerous examples can be found in the review chapter by Weitz [30]. These glassy states are particularly interesting from the technological standpoint, since they provide an avenue to manufacture a wide range of solid-like materials starting from colloidal solutions.

In this article we will revisit a particularly simple model of SALR system that can yield all types of cluster phases, and which was explored in some detail two decades ago by Im-

perio and Reatto [31–34]. The model, in which both attractive and repulsive interactions are simple exponentials, i.e. Kac interactions[35], was initially introduced in this context by Sear and coworkers[9] to account for the spontaneous patterning of quantum dots at the air-water interface. Later, Archer and coworkers [14, 22] used density functional theory and extensive Monte Carlo simulations to explore its phase behavior and map its corresponding phase diagram. Integral equations have also been applied to study this SALR potential in the homogeneous region [20]. In the comprehensive work of Archer and Wilding [22], in addition to the vapor-liquid transition, two first order transitions were identified depending on the packing fraction. Namely, a phase change at high dilution between a vapor and a fluid of liquid-like spherical clusters (globular cluster phase), and another transition between a liquid and fluid of spherical voids (bubble cluster phase). In this paper we will focus solely on the first instance. Interestingly, the same Kac-potential model was later used by Meyra and coworkers [36, 37] to explain the formation of vegetation patterns in environments with limited resources. This illustrates how SALR effective interactions can provide a qualitative (and even quantitative) explanation for spontaneous patterning over various orders of magnitude in the spatial (and to some extent temporal) dimension. In addition to the aforementioned studies in the bulk, Bores et al. [38, 39] also performed simulations and theoretical studies on the influence of confinement in disordered media on the pattern formation for the same SALR model. As mentioned, of all the possible cluster phases we will address the formation of the low density globular cluster phase, with an interaction and thermodynamics conditions tuned to yield relatively large clusters. These could actually represent a crude model of MLOs. Using large scale simulations we have analyzed the cluster size distributions, the intercluster and intracluster microscopic structure and dynamics illustrating their dependence on the thermodynamics conditions. The presence of two well separated spatial and temporal scales will be made evident.

As a consequence of the long range of the net inter-cluster interactions and relatively large attractive interparticle interaction (a type-III SALR potential), at the lowest temperature/highest density studied, clusters end-up in the vicinity of a dynamically arrested state, which falls into the class of a cluster glassy phase[23]. This is apparent from the small magnitude of both particle and the cluster diffusivities, as well as in the small frequency behavior of the frequency spectrum. Moreover, in these conditions, the second peak of the cluster-cluster pair distribution function exhibits a splitting which is a characteristic feature

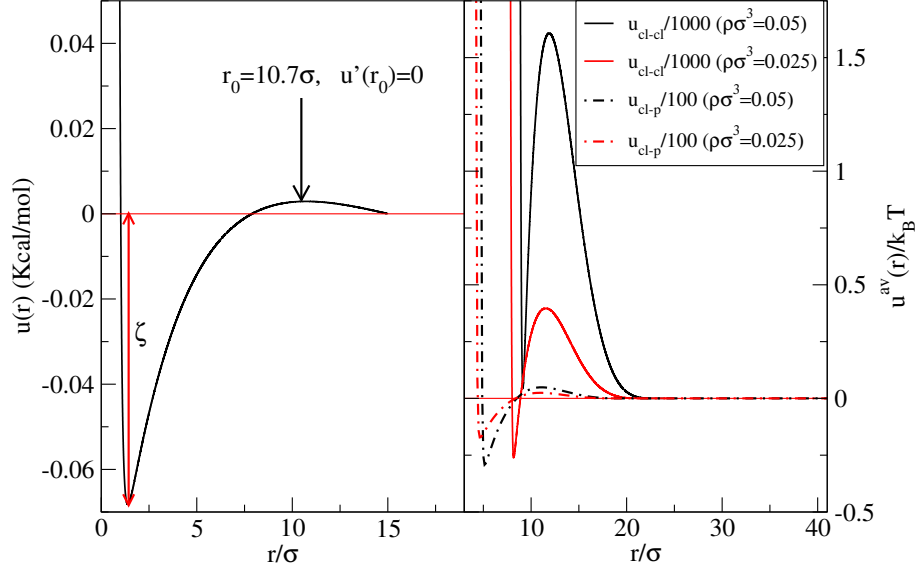


FIG. 1. Left) SALR interaction potential as described by Eq. (3). Right) Average intercluster potential (solid curves) and cluster-particle potential (dashed curves), computed assuming a uniform average cluster density and spherical cluster radii.

of dense amorphous materials (e.g metallic glasses [40]). We will see that the intercluster structure factor displays a strong attenuation of density fluctuations for a significant region of small wavenumbers. The system presents characteristics of a stealthy disordered hyperuniform material[41–43], i.e. due to the significant suppression of density fluctuations for a certain region of large wavelengths, the material becomes to some extent “invisible” to the corresponding radiation probes. The presence of an additional region with some attenuation for much shorter wavelengths (reflecting intracluster correlations) indicates that, to a smaller degree, it might be possible to have some sort of “stealthiness” for higher frequencies. This might have important implications in the field of optics and materials science.

The rest of the paper is sketched as follows. In the next section we will describe the SALR model and the simulation conditions. The single cluster structure (cluster size distributions, density profiles, average life times) and dynamics will be reviewed in Section IV. Two-particle and intercluster correlations are commented upon in Section V. The article is closed with a summary of our most relevant conclusions and future prospects.

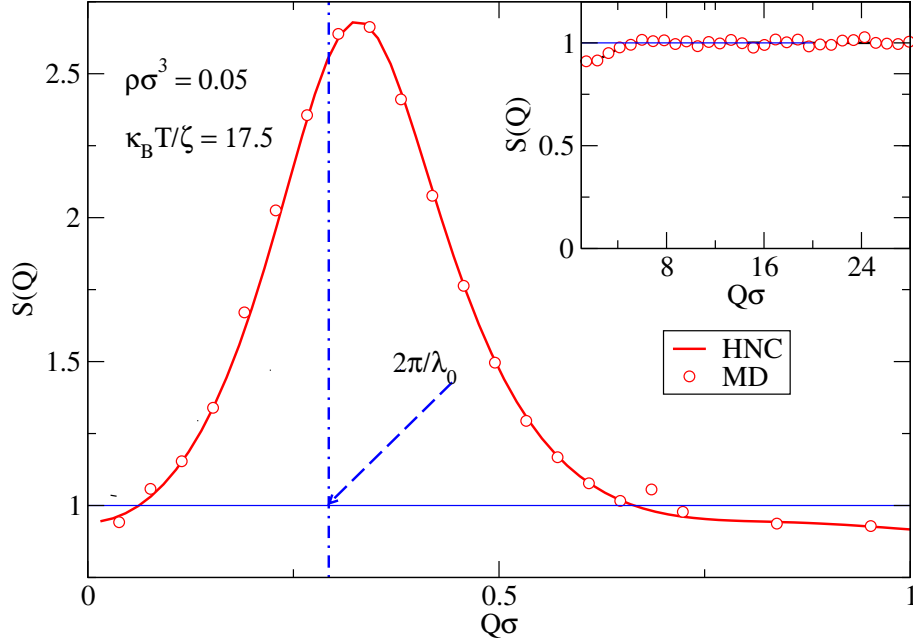


FIG. 2. High temperature structure factor from our HNC calculations (lines) vs MD results (symbols). In these conditions the system is in the homogeneous phase displaying the initial formation of aggregates. A vertical line marks the position of $2\pi/\lambda_0$,

II. MODEL AND METHODS

As mentioned in the Introduction the particles in our model will be interacting via a two-exponential Kac potential of the form used in Refs. [9, 14, 19, 22, 31, 38] to which we have added a soft core as in Ref.[38] in order to facilitate the use of molecular dynamics, namely

$$u^{SALR}(r) = \varepsilon \left[K_r e^{-\alpha_r r/\sigma} - K_a e^{-\alpha_a r/\sigma} + \left(\frac{\sigma}{r}\right)^{10} \right]. \quad (1)$$

Here σ is a measure of the inner particle core diameter and will be used as unit length. Since this is a rather soft potential, the actual size, as estimated from the particle-particle distribution function is $\sigma_{eff} \approx 0.8\sigma$. As mentioned by Sear and coworkers[9], while the use of the attractive exponential can be justified as a more or less crude modelization of dispersive forces as in the classical works by Kac et al.[35, 44], the repulsive exponential is used solely for the sake of computational simplicity. Thus, with $K_a, K_r > 0$, and $\alpha_a > \alpha_r > 0$ one has the characteristics of a SALR potential with the presence of a maximum for a distance r_0

larger than that corresponding to the potential minimum, whose analytical expression reads

$$r_0 = \frac{\sigma}{\alpha_a - \alpha_r} \log \frac{\alpha_a K_a}{\alpha_r K_r}. \quad (2)$$

The effect of the inner repulsive core on the value of r_0 is negligible. r_0 is a very significant correlation distance, that in the case of globular clusters determines roughly the cluster size. As will be explained below, due to the long range character of the interaction the average intercluster distance is twice as large, i.e. $\lambda_0 = 2r_0$. For lamellar phases, λ_0 determines the modulation distance, and in the bubble phase the average distance between the bubbles. In all cases the signature of this correlation length, λ_0 , is the presence of high intensity peak in the structure factor, $S(Q)$, located at $Q_m \approx 2\pi/\lambda_0$. For computational convenience the potential has been truncated and shifted at $R_c = 60\sigma$, i.e., we will be dealing with an interaction given by

$$u(r) = \begin{cases} u^{SALR}(r) - u^{SALR}(R_c) & \text{if } r \leq R_c \\ 0 & \text{if } r > R_c \end{cases} \quad (3)$$

Setting $K_r = 1$ and $K_a = 2$, $\sigma = 4 \text{ \AA}$, $\varepsilon = 0.1 \text{ kcal/mol}$, $\alpha_r = 0.1$ and $\alpha_a = 0.25$ one gets the potential depicted in the left graph of Figure 1. With this choice of parameters $r_0 = 10.7\sigma$ which, as mentioned above, determines the cluster diameter, as will be further confirmed in the next Section when discussing the average cluster density profiles. We will consider systems at relatively low number densities in order to guarantee the formation of micellar-like phases. Two total densities will be studied, $\rho\sigma^3 = 0.025, 0.05$.

The fact that the correlation length is twice the position of the potential maximum is easily understood in the case of globular clusters. In this instance one can assume a uniform effective density, ρ_{cl}^{eff} , inside the spherical clusters of effective radius R_{cl}^{eff} . These two quantities can be considered as optimization parameters in a Reverse Monte Carlo procedure[45], in which the interaction potential is computed from

$$u_{cl-cl}^{av}(r; \rho_{cl}^{eff}, R_{cl}^{eff}) = \left(\rho_{cl}^{eff}\right)^2 \int_{V_{cl}} d\mathbf{r}_1 \int_{V_{cl}} d\mathbf{r}_2 u(|\mathbf{r} - \mathbf{r}_1 + \mathbf{r}_2|) \quad (4)$$

with the objective function being the intercluster pair distribution. We have performed these calculations for the aforementioned densities. With the temperature defined as $k_B T/\zeta$ in terms of the potential well depth, ($\zeta = 0.068 \text{ kcal/mol}$, see Figure 1), k_B being Boltzmann's constant, the cluster-cluster potentials have been evaluated for the lowest temperature considered, $k_B T/\zeta = 3$. The double volume integrals over the cluster volumes are carried

out numerically using a Gauss-Legendre quadrature, with $u(r)$ given by Eqs. (1) and (3). With this procedure we end up with estimated effective cluster densities of $\rho_{cl}^{eff}\sigma^3 = 1.2$ ($\rho\sigma^3 = 0.05$) and 0.83 ($\rho\sigma^3 = 0.025$), with corresponding effective radii, $R_{cl}^{eff}/\sigma = 4.5$, and 4, respectively. The results obtained from Eq. (4) are presented in the right graph of Figure 1. The dashed curves correspond to the cluster-particle interaction that is simply obtained by removing one of the effective cluster densities and one volume integration from Eq. (4). We see in the Figure that the net inter-cluster interaction is extremely repulsive, orders of magnitude more intense than the interparticle potential, and dies out approximately at $\lambda_0 = 2r_0$. This explains why this correlation length determines the intercluster separation, as will be explicitly reflected by the first peak of the cluster-cluster pair distribution that will be discussed in the next section. Note that this is not a consequence of the cut-off introduced in (3) for computational convenience since $R_c \approx 3\lambda_0$. It is the competition between attractive and repulsive components what cancels most of both the cluster-cluster and (to a lesser extent) the cluster-particle interactions at approximately λ_0 . Interestingly, our spherical clusters act like large repulsive spheres of approximate diameter λ_0 whereas their actual diameter (the precise value depends on the definition as we will see) is $\approx \lambda_0/2$, i.e. the excluded volume is 2^3 times the average cluster volume.

Molecular dynamics simulations have been run specifically in the NVT ensemble using the LAMMPS package[46] for a total of 218000 particles of mass 100 amu. Distance and energy units for the simulation have been chosen following the LAMMPS package *real* units specification. The integration time step was set to 2 fs. Results will be presented in terms of reduced units, both for temperature (defined in terms of the well depth as indicated above), length (using $\sigma = 4\text{\AA}$ as unit length) and time, for which the time unit is given by $\tau_0 = (m\sigma^2/\zeta)^{1/2} = 7.5\text{ps}$. The systems were equilibrated for 20 ns, of which the first 10 ns correspond to a slow cooling process following a linear temperature ramp starting from a fully disordered system at $k_B T/\zeta = 18$ down to the desired temperatures, namely, $k_B T/\zeta = 3, 6, 9, 12$, and 15 for $\rho\sigma^3 = 0.05$ and just $k_B T/\zeta = 3$, and 9 for $\rho\sigma^3 = 0.025$. It is worth stressing that shorter equilibration runs (5 ns) lead to very similar cluster size/radii distributions. This is an indication that the results presented correspond to equilibrium states. For much shorter equilibration runs and/or cooling times it is very easy to end up with bimodal or even multi-modal cluster size/radii distributions. Production runs were $\tau_{run} = 20\text{ns}$ long with configurations stored every 10 ps.

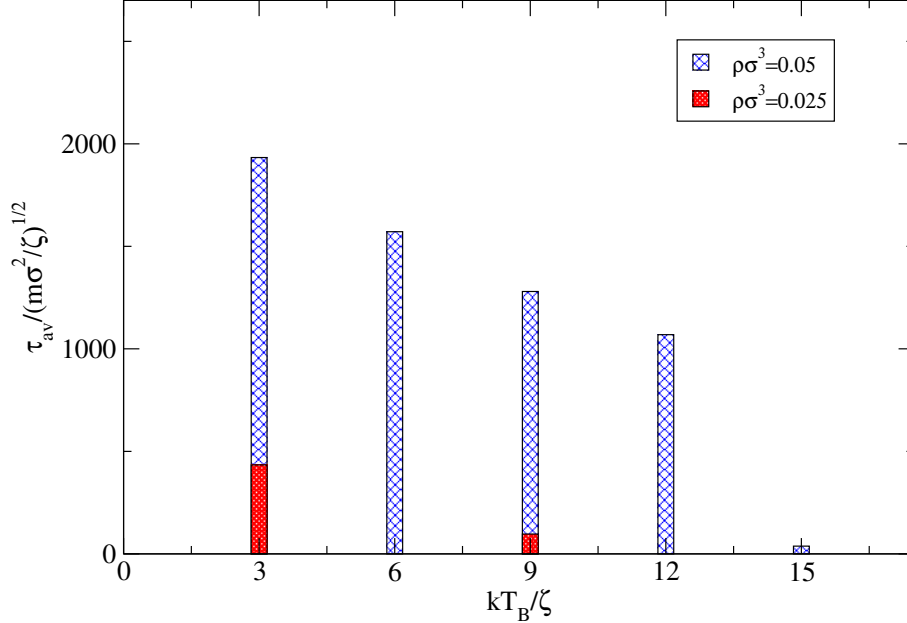


FIG. 3. Average life time of the clusters, (τ_{av} , red bars) as a function of temperature for $\rho\sigma^3 = 0.05$ (blue bars) and $\rho\sigma^3 = 0.025$ (red bars). The upper limit of the y -axis corresponds to the length of the simulation production run, τ_{run} .

III. ONSET OF CLUSTERING

As mentioned before, we have chosen potential parameters and thermodynamic conditions for the system to yield a globular cluster phase. We have first explored a series of temperatures for the two densities indicated above using the Hypernetted Chain integral equation [47]. As shown by Archer and Wilding[22] this equation has a non-solution region which hides the cluster phase. This lack of solutions (in fact solutions have analytical continuation in the complex space[48]) can be interpreted as a signature of a phase transition, in this instance a first order transition between the particle gas and a fluid of liquid-like spherical clusters. In our case we find that real solutions for the largest density disappear below $k_B T_{ns}^{HNC}/\zeta = 14.9$, and $k_B T/\zeta = 8$ for $\rho\sigma^3 = 0.025$. For $k_B T_c/\zeta = 17.5$ and $\rho\sigma^3 = 0.05$ the HNC converges yielding a structure factor in excellent agreement with the simulation (cf. Figure 2). A visual inspection of simulation snapshots does not show evidence of clustering. Interestingly, in Figure 2 we first see that for this temperature there is a significantly high prepeak (also known as intermediate range order peak [24]) which reaches the value $S(Q_m) \approx 2.7$ for $Q_m \approx 2\pi/\lambda_0$, whereas for $Q\sigma \gtrsim 1$ the structure factor

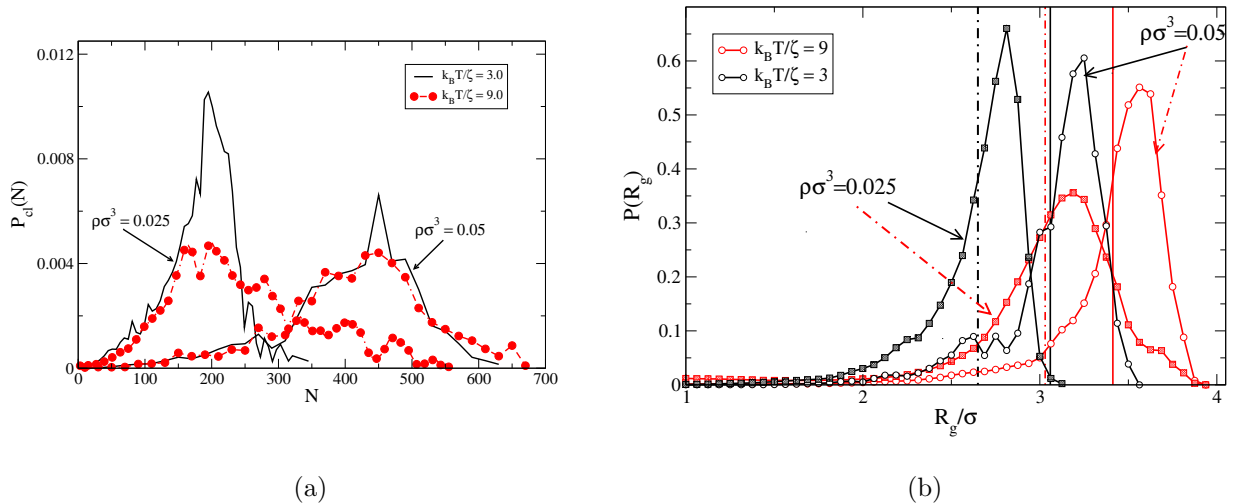


FIG. 4. a) Cluster size distribution dependence on temperature and global density b) Cluster radii of gyration distribution in terms of density and temperature. Average radii are indicated by vertical lines.

corresponds to that of a dilute gas of uncorrelated particles. Godfrin and coworkers propose the use of this precise value of the prepeak height as signature of the onset of the cluster phase[24]. We will see in the next sections that lowering the temperature increases the height of the prepeak by orders of magnitude, i.e. $S(Q_m)$ practically diverges for a $Q_m \neq 0$, which suggests the existence of a non-zero Lifshitz point[20]. This means that the system becomes unstable with respect to a modulated inhomogeneous phase, whose modulation is given by $Q_m \approx 2\pi/\lambda_0$. The locus of Lifshitz points for varying densities yields the λ -line [22], a term borrowed from the study of criticality in ionic fluids[49]. It must be mentioned, that Bollinger and coworkers[50] suggested the use of an additional criterion to characterize the onset of the cluster phase, namely, a thermal correlation length with values within the interval $2 \lesssim \xi_T/\sigma \lesssim 3$. This quantity can be estimated from a Lorentzian fit of the prepeak, which in our case yields $\xi_T/\sigma = 5.6$, exceeding the limit suggested in Ref. [50]. However, one must bear in mind that Ref. [50] is focused on Yukawa (screened Coulomb) interactions, and here we are dealing with bare exponentials. So far it has not been assessed to what extent the choice of the explicit form of the potential affects the reliability of this criterion. Until a complete analysis of the type performed in Ref. [50] is carried out it seems reasonable to stick to Godfrin's et al choice.

IV. SINGLE-CLUSTER STRUCTURE AND DYNAMICS

In order to define the clusters we have used a geometric criterion, namely, all those particles whose separation is below $d_{cl} = 1.3\sigma$ are considered as pertaining to the same cluster. This distance roughly corresponds to the first non-zero minimum of the particle-particle pair distribution function, i.e. it is an estimate of the outer boundary of the first coordination shell. Once this clustering distance was set, we have run a GPU density based parallel scan (G-DBSCAN [51]) using an in-house code. Specific GPU optimizations were performed to calculate structure factors, pair distribution functions [52–54] and dynamic properties. Only clusters containing more than 4 particles have been considered for the analysis below.

A first observation from our cluster analysis is the fact that the structures are long-lived. In Figure 3 the average cluster life time, τ_{av} is displayed for the thermodynamics states under consideration. The top of the ordinate axis corresponds to the length of the production run, $\tau_{run} \approx 2700\tau_0$. For the highest density, up until $k_B T/\zeta = 15$ the average lifetime exceeds half the length of the simulation, which is an indication of the stability of the structures. This is explained by the large depth of the cluster-particle potential (see right graph of Figure 1). At $k_B T_c/\zeta \approx 15$ the clusters are extremely short lived, this temperature being fairly close to the limit of real solutions of the Hypernetted Chain integral equation, which has been discussed above. For higher temperatures no significant clustering is found. Now, when the density decreases the average life time of the clusters decreases substantially. The real solution of the HNC disappears at $k_B T/\zeta = 7.6$, but for $k_b T/\zeta = 9$ the simulation results still display a significant degree of clustering, although much more short lived. Simulation runs for higher temperatures (results not included) do not show evidence of clusters satisfying our minimum size criterion.

As to the cluster statistics, in Figure 4 we present the cluster size distribution for the two densities in question and two selected temperatures (left graph) and the corresponding cluster radii distributions depicted in the right graph. As estimate of the cluster radii we have used the value of the gyration radius, which is defined in the usual fashion [55] by

$$R_g = \left\langle \sqrt{\frac{\sum_i m_i (\mathbf{r}_i - \mathbf{R}_{com})^2}{\sum_i m_i^2}} \right\rangle \quad (5)$$

where the brackets indicate a ensemble average and \mathbf{R}_{com} is the center of mass of the cluster

whose radius of gyration is being computed. We see that for the largest density the size distribution peaks at around 450 particles and at 200 particles for the lowest. For all temperatures the clusters are liquid droplets, as will be illustrated below when analyzing the short time behavior of the mean square displacement.

Interestingly one can see that the shape of the cluster size distribution is hardly affected by temperature in the case of the largest density, whereas for low density becomes much wider and much larger clusters appear as temperature rises. This, in combination with the short lifetime of the clusters seen in Figure 3, is an indication of a rapid merging and splitting of clusters taking place for the lower density/high T case. The large spread of the low density-high T size distribution is also reflected in the cluster radii distribution, which in this case is almost Gaussian-like. All remaining distributions are negatively skewed beta-distributions with a more or less wide hump at approximately one particle diameter below the maximum of $P(R_g)$. This probably results from the tendency of clusters to free and recapture their external layer of particles. This is more difficult for internal layers where particles are strongly attached, except for the low density/high temperature case. Here

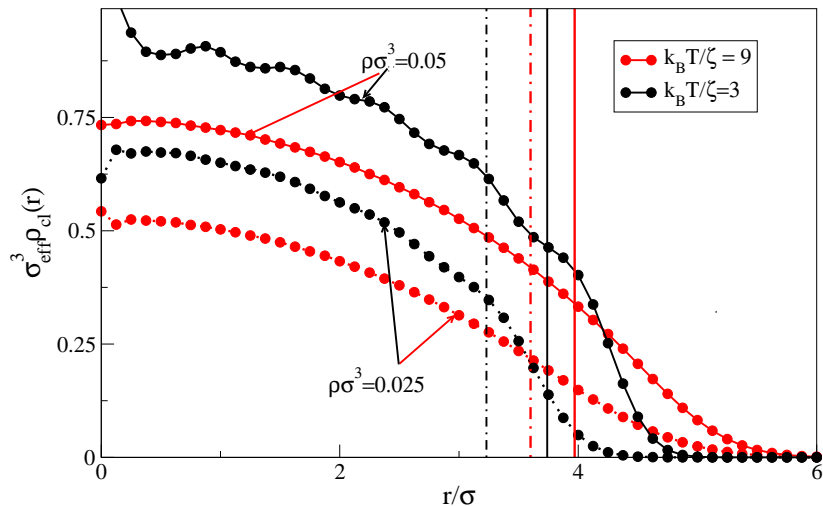


FIG. 5. Temperature and density dependence of the average density profile of the clusters. Densities have been scaled with the effective diameter of the particles which is $\sigma_{eff} \approx 0.8\sigma$. Vertical lines denote the radii corresponding to the Gibbs dividing surface (cf. Eq. (6) in the text).

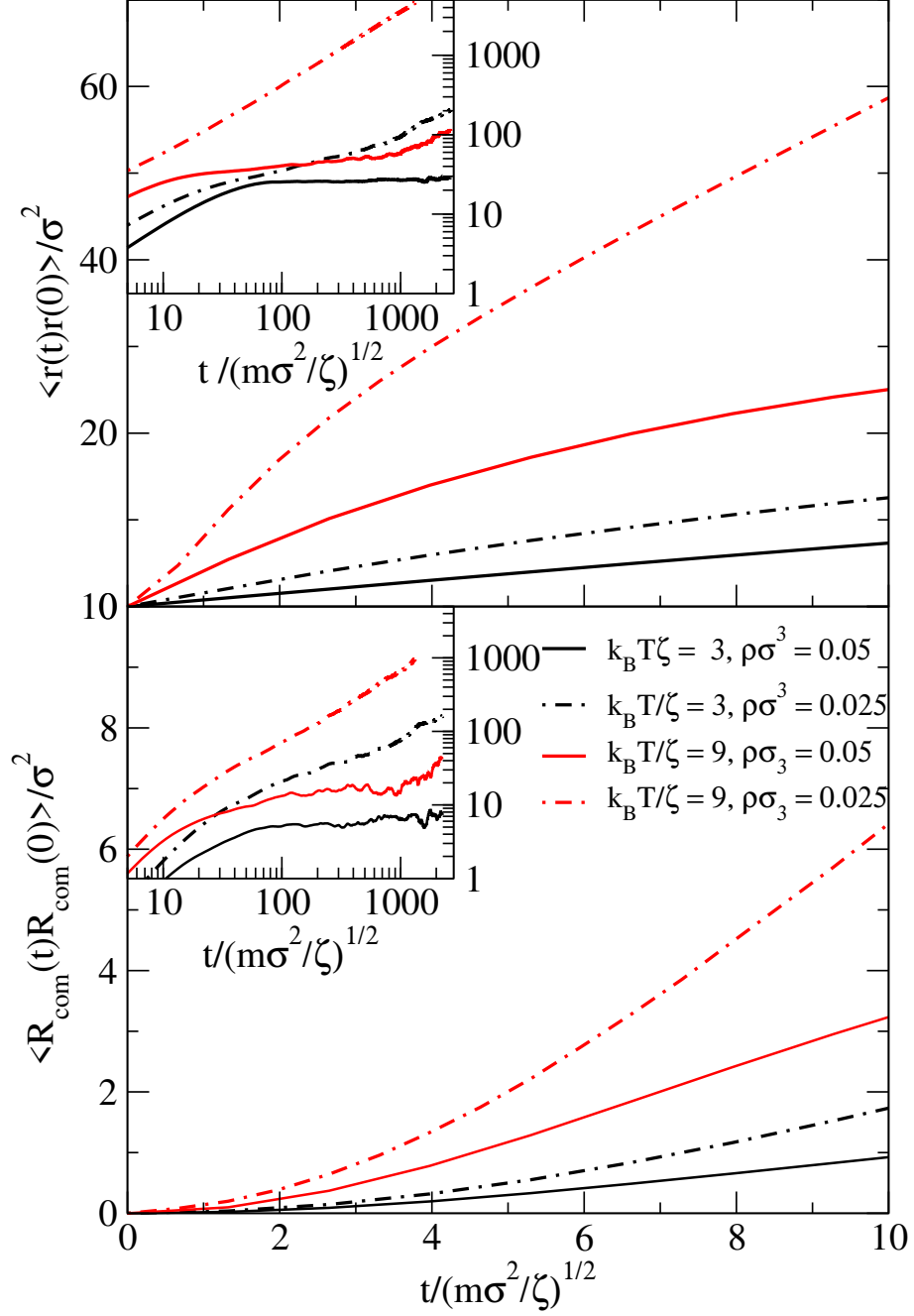


FIG. 6. Upper graph) Single particle mean square displacement dependence of temperature and density. Lower graph) Density and temperature dependence of the center of mass mean square displacement for persistent clusters. In both graphs velocities and time are expressed in reduced units.

dominates the thermal equilibrium between destruction and creation of clusters leading to the Gaussian-like distribution.

This picture is complemented by an inspection of the cluster average density profiles, $\rho_{cl}(r)$, depicted in Figure 5. In this case, we have scaled the densities with $\sigma_{eff} = 0.8\sigma$ in order to be able to compare the densities with those of standard fluids (e.g. for a Lennard-Jones fluid, liquid densities are usually assumed to be $\rho\sigma^3 \gtrsim 0.4$). One first notices that despite the extremely low total particle densities, for $\rho\sigma^3 = 0.05$ the clusters display very high values of the effective density profile, even for high T. These values are well into the liquid domain. For the lower global density, the effective inner cluster density remains almost within the boundaries of the liquid state. In both cases there is a transition towards gas-like densities as the profile approaches the surface in a gradual fashion. Taking into account that the clusters are rather spherical, we have defined a Gibbs dividing surface in order to have a quantitative description of the separation between gas-like particles and liquid-like particles, as is customary in the description of gas-liquid interfaces [47]. This quantity places an ideal separation between the gas-like cluster region from its corresponding liquid-like counterpart. Here, for a spherical cluster this should be the surface of a sphere, whose radius (Gibbs dividing radius) R_{Gibbs} is given by

$$\int_0^{R_{Gibbs}} r^2(\rho_{cl}(0) - \rho_{cl}(r))dr = \int_{R_{Gibbs}}^{\infty} r^2\rho_{cl}(r)dr. \quad (6)$$

Obviously, when one has a uniform density, $\rho_{cl}(r) = \rho_{cl}(0)$ with a sharp interface at R_{Gibbs} , both sides of Eq. (6) are identically zero.

We see that this Gibbs radii separating gas-like and liquid-like particles in the clusters (vertical lines in Figure 5) follow the same trends as the average radii of gyration (vertical lines in Figure 4(b)), i.e. larger values for larger densities, and for the same density the radius increases with temperature. This latter trend reflects the larger spread of the cluster size distributions as temperature raises. The Gibbs radii are systematically larger ($\approx 0.5\sigma$) than the gyration radii. This is a consequence of the lesser weight of the “gas atmosphere” surrounding the quasi-spherical clusters in Eq. (5). It is worth noticing that the cluster density profiles reach vanishing values in the interval $4.5\sigma < r < 5.5\sigma$, by which the average cluster spatial extent is $\lesssim \lambda_0$.

Now a few words concerning the single particle dynamics. In what follows, in order to make the results independent of specific details of the model, time and frequency will be

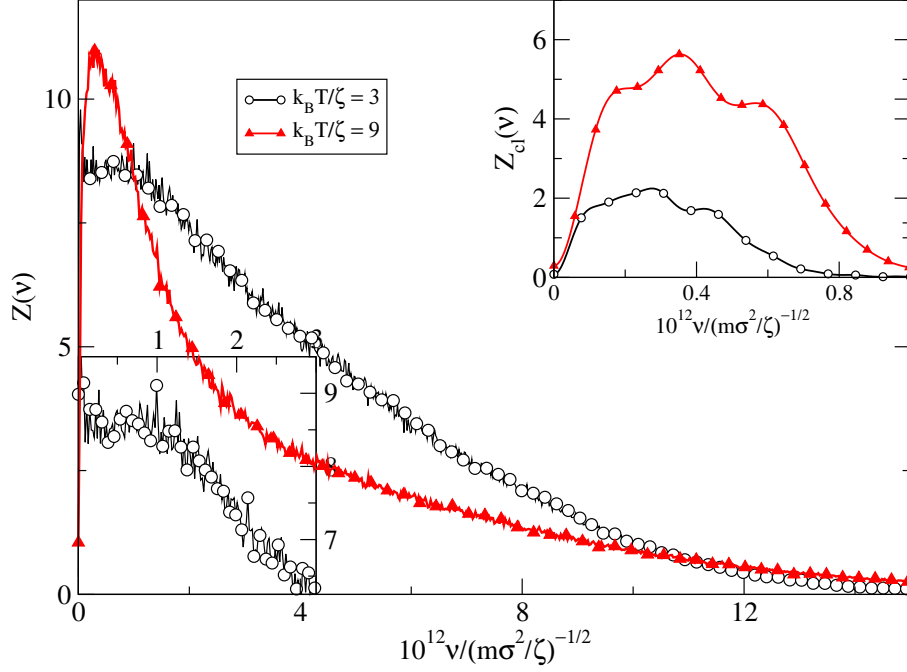


FIG. 7. Vibrational frequency spectra derived from the particles velocity self-correlation at various temperatures and $\rho\sigma^3 = 0.05$, and the cluster vibrational frequency spectrum (inset in lower graph) as computed from the velocity self-correlation of the persistent clusters centers of mass.

reduced with the corresponding molecular time unit, τ_0 and its inverse τ_0^{-1} respectively. Here we first look at the individual particle mean square displacement (m.s.d), plotted in the upper graph of Figure 6. It is apparent from the figure that there are clearly two separate regimes. First, a short time scale (under $10 \tau_0$, i.e. for our system around 70ps) where the system is in a diffusive regime corresponding to intracluster movements. This regime can be split into two more or less linear regions with a decreasing diffusion constant (slope of the curves). This reflects the finite size of the clusters. For much longer times (up to $2.7 \times 10^3 \tau_0$) the behavior of the mean square displacement is represented in the inset. We observe for the low density-high temperature case a fully linear behavior, with the m.s.d. exhibiting the steepest slope, i.e. the largest diffusivity. Except for the high density-low temperature case the two remaining cases display a plateau after the initial diffusive regime followed by a long time diffusive behavior. In this latter region the mean square displacement grows rather linearly as well. This is contrast with the higher density-low temperature case in which the plateau extends for the duration of the simulation. This long time behavior stems mostly from the collective cluster movement which is shown in the lower graph of Figure

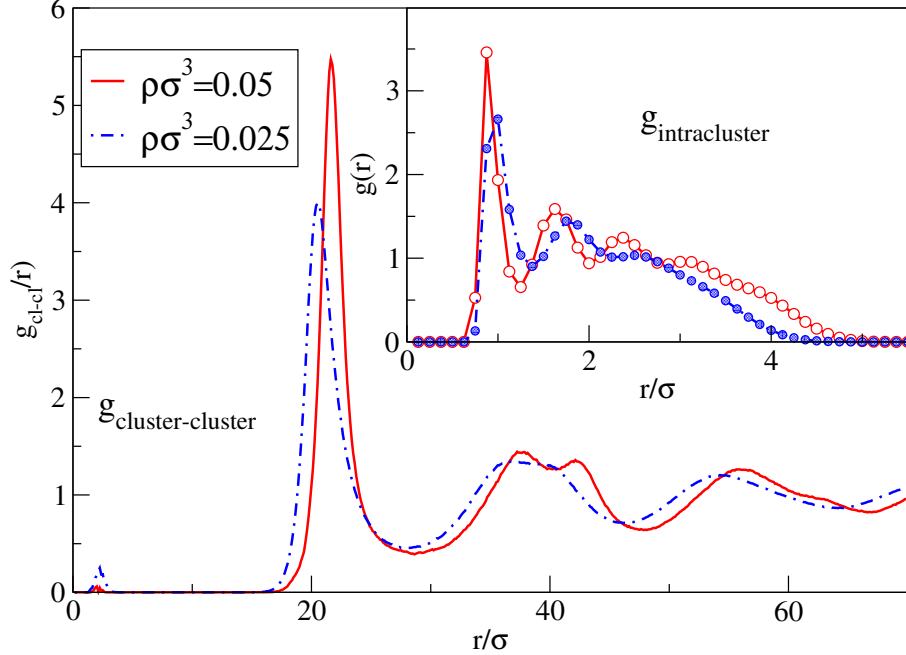


FIG. 8. Cluster-cluster pair distribution function and intra-cluster pair distribution function (inset) for the lowest temperature state $k_B T/\zeta = 0.3$.

6. Here we have plotted the mean square displacement of the center of mass of persistent clusters, that is, those that preserve their identity during the length of the production run, neither splitting nor merging with other clusters. At short times one can even appreciate the ballistic regime with a parabolic m.s.d. before the clusters begin to collide. We see that the long time behavior (inset) displays the same trends as the single particle mean square displacement, but one can actually measure a tiny diffusivity for the clusters at higher density/low temperature, namely $D/(\sigma^2\zeta/m)^{1/2} = 0.0003$. This is an indication that our system is approaching an arrested glassy state. Taking into account that the source of this quasi-freezing of the cluster positions is mostly induced by the long range of the repulsive interactions (cf the right graph of Fig. 1) one is tempted to identify this state as a precursor of a Wigner glass of clusters[26]. However, strictly speaking the formation of Wigner crystals and glasses [56] is due to extremely long ranged interactions such a Coulombic ones, in conjunction with higher packing fractions. Following the discussion of Klix and coworkers [23] and bearing in mind the significant interparticle attraction of our model and low packing fraction, we are probably somewhere near the dynamic transition towards a cluster glassy state.

These features are further confirmed by an analysis of the velocity self-correlation functions (not represented for the sake of brevity). In the case of the low T-high density clusters there is a well separated time regime in which the particles within the cluster experience the “cage effect”, i.e. density is sufficiently high for the particles to reverse direction due to collisions with the nearest neighbors. This is less apparent as temperature increases and density is lowered. These effects are reflected in the vibrational frequency spectrum, which is the Fourier transform of the particle velocity self-correlation function in the time domain. This quantity is depicted in Figure 7 for low and high temperatures and the largest density, both for the single particle dynamics and in the inset for that of the centers of mass of persistent clusters, $Z_{cl}(\nu)$. Thus, concerning particle diffusivities, these correspond to the values of $Z(0)$ (with our convention for the velocity autocorrelation $Z(0) = D$). In agreement with the behavior of the m.s.d. (cf. Figure 6), diffusivity increases with temperature, and we see that from the point of view of the particle dynamics the system is fluid-like. At the lowest temperature we observe a small secondary maximum close to $\nu \approx 10^{-12}\tau_0^{-1}$ (cf. lower inset in Figure 7): this corresponds to “vibrational” movements due to particle collisions inside the clusters, i.e. the aforementioned “cage” effect. The first maximum that occurs at $\nu \approx 0.5 \times 10^{-12}\tau_0^{-1}$ for the highest temperature is connected with translational excitations, and it shifts to lower frequencies as temperature is decreased. .

In the inset we present the vibrational spectra obtained from the cluster’s center-of-mass velocity self-correlation. It displays very definite peaks at substantially low frequencies. These peaks correspond to collective cluster vibrations around the equilibrium positions that are almost frozen into an arrested state, as can be inferred from their relatively low diffusivities, both computed from the long time limit of the m.s.d. and from $Z_{cl}(0)$ in Figure 7. The effect of temperature for the density in question on the cluster dynamics is precisely to increase the intensity of the collective vibrations of the clusters. Obviously, for $k_B T/\zeta > 15$ this spectrum vanishes due to the dissociation of the aggregates and subsequent melting of the cluster fluid into a low density homogeneous fluid.

V. TWO-PARTICLE AND INTERCLUSTER STRUCTURAL CORRELATIONS

We can now analyze two-particle correlations. To start with, in Figure 8 we present the cluster-cluster pair distribution function for the lowest temperature and the two densities

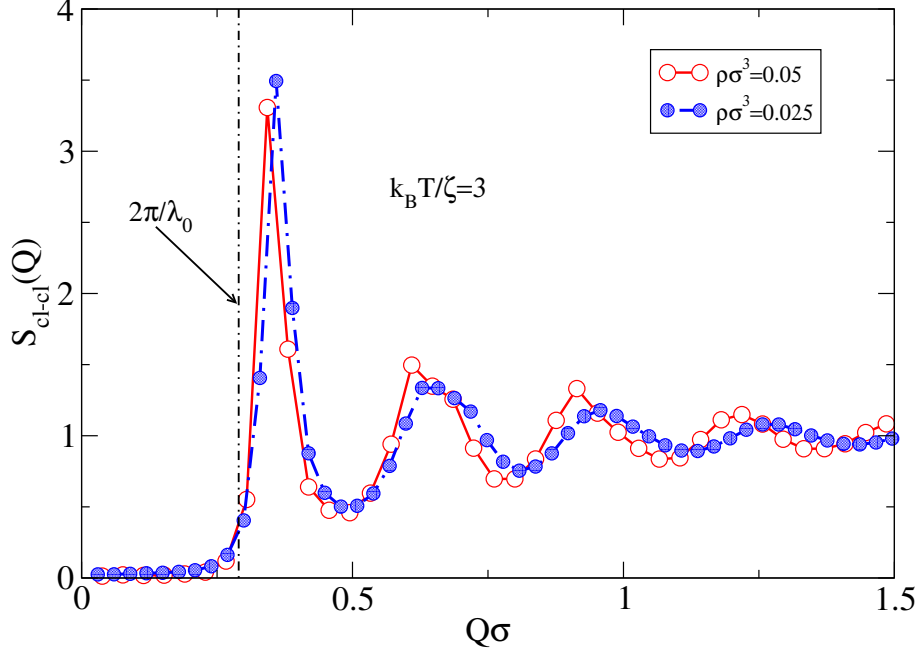


FIG. 9. Cluster-cluster structure factor for the lowest temperature state $k_B T/\zeta = 0.3$.

under consideration. In the inset the corresponding particle-particle intracluster pair distribution functions are shown. Our previous discussion concerning the average intercluster potential (cf. right graph in Figure 1) explains that clusters are separated by the correlation length $\lambda_0 \approx 20\sigma$. The smaller size of the clusters for low density implies the shift of the first peak of $g_{cl-cl}(r)$ to lower distances. The splitting of the second coordination shell for $\rho\sigma^3 = 0.05$ is a typical signature of the presence of an amorphous structure[40], although in our case there is a residual diffusivity. Interestingly, this feature is found in dense amorphous systems, but in contrast here, the total density is very low ($\rho\sigma^3 = 0.05$). Nonetheless, we must bear in mind that the excluded volume of the clusters is much larger than what would correspond to their actual size, as previously discussed. Thus, for instance, Figure 8 is obtained from a total of $N_{cl} \approx 500$ clusters in a cubic box of side $L=165\sigma$. If one uses as rough estimate of the effective cluster diameter the position of the first maximum of g_{cl-cl} , $\sigma_{cl}^{eff} \approx 20\sigma$, the effective density of clusters is $N_{cl}\sigma_{cl}^{eff3}/L^3 \approx 0.9$ which is certainly very high. As we have seen, the effective diameter is approximately twice the spatial extent of the clusters, due to the long range repulsion of the interaction 1. On the other hand, once the density is halved the splitting disappears.

As to the intracluster pair distribution function, its decay beyond 3σ is a consequence of

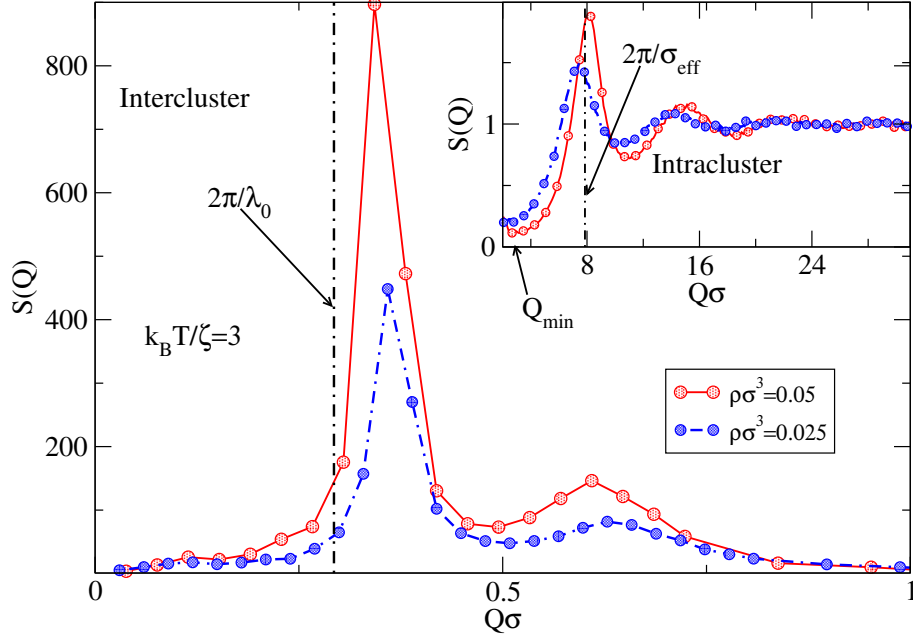


FIG. 10. Temperature and density dependence of the total structure factor $S(Q)$ (main graph) and the intracuster structure factor (inset) for the system in stable cluster phases.

the finite averaged cluster size (cf the density profiles of Figure 5) but its liquid-like structure is very remarkable, with a first coordination shell reaching considerably high values. From the position of the first peaks and their decay towards shorter interparticle separations, one can appreciate that the potential core is relatively soft, and that is the reason why we have considered an effective particle diameter $\sigma_{eff} \approx 0.8\sigma$. A steeper repulsion in Eq. (1) (e.g. a Lennard-Jones r^{-12} term) would bring the effective size closer to σ , but this would require a finer grid in the potential interpolation used in the LAMMPS package[46] which might lead to memory exhaustion in the GPUs.

If we now move from real to Fourier space, in Figure 9 we have the cluster-cluster structure factor, $S_{cl-cl}(Q)$. A first feature is to be noted, the height of the first peak for both densities is beyond Hansen-Verlet's[57] freezing rule $S(Q_m) \gtrsim 2.86$ for which a transition towards a crystal is to be expected. As discussed above, our system presents features of an amorphous solid, but with a somewhat peculiar structure factor. We see that $S(Q) \approx 0, \forall Q \lesssim 0.2\sigma^{-1}$. In fact, one finds that the hyperuniformity index $H = S(Q_{max})/S(0 < Q \lesssim 0.2\sigma^{-1}) \approx 10^3 \sim 10^2$ is relatively high. While its value is still away from the criterion for *near hyperuniformity*, $H \gtrsim 10^4$ proposed by Atkinson and coworkers [58] in maximally random jammed systems, it represents a considerable attenuation of density fluctuations, and actually meets the criterion

of *effective hyperuniformity*, $H \gtrsim 10^2$ proposed by Chen and et al.[59]. Lowering the temperature and choosing a material with the appropriate scattering form factor will improve the hyperuniform and stealthy character of the material for wavenumbers below $0.2\sigma^{-1}$. Tuning the size of the constituent particles one could increase or decrease the wavenumber range of stealthiness.

We note that the positions of the first maximum of the structure factors deviate from the value estimated from the correlation length, $Q_m = 2\pi/\lambda_0$ (shown in the Figure by a vertical line), almost by 20%. Although the first peak of the intercluster pair distribution (Fig. 8) appears at $\approx \lambda_0$, the real effective cluster-cluster interaction is much softer than that depicted in the right graph of Figure 1. The particle density inside the clusters (cf. Figure 5) is far from the uniform density that was assumed in Eq. (4). This should lead to a softer outer range of the intercluster effective potential explaining the shift of Q_m with respect to $2\pi/\lambda_0$. The fact that $Q_m(\rho\sigma^3 = 0.05) > Q_m(\rho\sigma^3 = 0.025)$ reflects the smaller size of the clusters for the lower density (see the corresponding radii of gyration in Figure 4(b)) and matches the shift to lower r of the first maximum of g_{cl-cl} in Figure 8.

If we now look at the total structural factor, $S(Q)$ depicted in Figure 10, its most noticeable feature is the huge magnitude of the prepeak, which is the signature of a large degree of clustering. Obviously the prepeak positions correspond to that of the first maxima in the cluster-cluster structure factors discussed above. Also here the hyperuniformity index meets the criterion of *effective hyperuniformity*.

In the inset we can see the large wavenumber behavior of $S(Q)$. The peak maxima $Q_{max}\sigma \approx 8.1$ reflects interparticle correlations at 0.8σ , which is precisely the effective particle diameter, σ_{eff} . This is in accordance with the maxima of $g(r)$ in the inset of Figure 8. Interestingly, $H = S(Q_{max})/S(Q_{min}) = 0.2 \times 10^2$ which is not very far from the criterion of effective hyperuniformity. A proper choice of the short range interparticle interactions might actually drive the system closer to having an additional wavenumber range where density fluctuations should be heavily attenuated.

VI. CONCLUSIONS

In summary, we have presented a study of the structural and dynamic properties of a simple model of a type-III SALR self-associating fluid, focusing on the globular cluster phase.

Here we have studied both cluster size distributions, cluster density profiles, diffusion and frequency spectra as well as pair distributions (inter and intracluster) as well as structure factors. We have found that the cluster phase for moderate densities (still low packing fraction) as the temperature is lowered approaches a cluster glassy state. Interestingly, in these conditions the system shows a considerable attenuation of density fluctuations for a range of wavenumbers below $0.2\sigma^{-1}$, by which the material meets the criteria of *effective hyperuniformity and stealthiness*. Future work will focus on mixtures where intracluster phase separation can enable the tuning of anisotropic cluster-cluster interactions. At present, a two-dimensional counterpart of the system analyzed in this work is under study. An extension of the theoretical approach of Sweatman and coworkers[21] to include correlations at the HNC level so as to provide a more precise description of one and two-body cluster correlations is currently being developed.

ACKNOWLEDGMENTS

The authors acknowledge the support from the Agencia Estatal de Investigación and Fondo Europeo de Desarrollo Regional (FEDER) under grants No. PID2020-115722GB-C21 and PID2020-115722GB-C22. We also would like to acknowledge the Galicia Supercomputing Center (CESGA) for the access to their computer facilities.

-
- [1] A. Stradner, H. Sedgwick, F. Cardinaux, W. C. K. Poon, S. U. Egelhaaf, and P. Schurtenberger, *Nature* **432**, 492 (2004).
 - [2] A. Ciach, J. Pekalski, and W. T. Gozdz, *Soft Matter* **9**, 6301 (2013).
 - [3] Y. Liu, L. Porcar, J. Chen, W.-R. Chen, P. Falus, A. Faraone, E. Fratini, K. Hong, and P. Baglioni, *The Journal of Physical Chemistry B* **115**, 7238 (2010).
 - [4] E. Yearley, P. Godfrin, T. Perevozchikova, H. Zhang, P. Falus, L. Porcar, M. Nagao, J. Curtis, P. Gawande, R. Taing, I. Zarraga, N. Wagner, and Y. Liu, *Biophys. J.* **106**, 1763 (2014).
 - [5] N. Kovalchuk, V. Starov, P. Langston, and N. Hilal, *Adv. Colloid Interfac.* **147–148**, 144 (2009).
 - [6] M. B. Sweatman and L. Lue, *Advanced Theory and Simulations* **2**, 1900025 (2019).

- [7] T. Hirose, K. Ninomiya, S. Nakagawa, and T. Yamazaki, *Nat. Rev. Mol. Cell Biol.* **24**, 288 (2022).
- [8] A. C. Murthy and N. L. Fawzi, *Journal of Biological Chemistry* **295**, 2375 (2020).
- [9] R. P. Sear, S.-W. Chung, G. Markovich, W. M. Gelbart, and J. R. Heath, *Phys. Rev. E* **59**, R6255 (1999).
- [10] M. A. Boles, M. Engel, and D. V. Talapin, *Chemical Reviews* **116**, 11220 (2016).
- [11] H.-N. Barad, H. Kwon, M. Alarcón-Correa, and P. Fischer, *ACS Nano* **15**, 5861 (2021).
- [12] D. Andelman, F. Broçhard, and J.-F. Joanny, *The Journal of Chemical Physics* **86**, 3673 (1987).
- [13] M. Seul and D. Andelman, *Science* **267**, 476 (1995).
- [14] A. J. Archer, D. Pini, R. Evans, and L. Reatto, *J. Chem. Phys.* **126**, 014104 (2007).
- [15] S. Mossa, F. Sciortino, P. Tartaglia, and E. Zaccarelli, *Langmuir* **20**, 10756 (2004).
- [16] Y. Liu and Y. Xi, *Current Opinion in Colloid & Interface Science* **39**, 123 (2019).
- [17] A. J. Archer, *Phys. Rev. E* **78**, 031402 (2008).
- [18] A. J. Archer, C. Ionescu, D. Pini, and L. Reatto, *J. Phys.: Condens. Matter* **20**, 415106 (2008).
- [19] J.-M. Bomont, J.-L. Bretonnet, D. Costa, and J.-P. Hansen, *J. Chem. Phys.* **137**, 011101 (2012).
- [20] J.-M. Bomont and D. Costa, *J. Chem. Phys.* **137**, 164901 (2012).
- [21] M. B. Sweatman, R. Fartaria, and L. Lue, *J Chem Phys.* **140**, 124508 (2014).
- [22] A. J. Archer and N. B. Wilding, *Phys. Rev. E* **76**, 031501 (2007).
- [23] C. L. Klix, C. P. Royall, and H. Tanaka, *Physical Review Letters* **104**, 165702 (2010).
- [24] P. D. Godfrin, N. E. Valadez-Pérez, R. Castañeda-Priego, N. J. Wagner, and Y. Liu, *Soft Matter* **10**, 5061 (2014).
- [25] Y. Zhuang and P. Charbonneau, *J. Phys. Chem. B* **120**, 6178 (2016).
- [26] J. Ruiz-Franco and E. Zaccarelli, *Annu. Rev. Condens. Ma. P.* **12**, 51 (2021).
- [27] I. Palaia and A. Šarić, *J. Chem. Phys.* **156**, 194902 (2022).
- [28] J. Bosse and S. D. Wilke, *Phys. Rev. Lett.* **80**, 1260 (1998).
- [29] K. A. Dawson, *Current Opinion in Colloid & Interface Science* **7**, 218 (2002).
- [30] D. A. Weitz, “Glasses and grains,” (Birkhauser, 2011) Chap. Colloidal Glasses, pp. 25–38.
- [31] A. Imperio and L. Reatto, *J. Phys.: Condens. Matter* **16**, S3769 (2004).

- [32] A. Imperio and L. Reatto, *J. Chem. Phys.* **124**, 164712 (2006).
- [33] A. Imperio, D. Pini, and L. Reatto, in *International Workshop on Collective Phenomena in Macroscopic System* (Villa Olmo, Como, Italy, 2006).
- [34] A. Imperio and L. Reatto, *Phys. Rev. E* **76**, 040402(R) (2007).
- [35] M. Kac, *Phys. Fluids* **2**, 8 (1959).
- [36] A. G. Meyra, G. J. Zarragoicoechea, and V. A. Kuz, *Mol. Phys.* **110**, 173 (2012).
- [37] A. G. Meyra, G. J. Zarragoicoechea, and V. A. Kuz, *Physical Review E* **91**, 052810 (2015).
- [38] E. Lomba, C. Bores, and G. Kahl, *J. Chem. Phys.* **141**, 164704 (2014).
- [39] C. Bores, N. Almarza, E. Lomba, and G. Kahl, *J. Phys. : Condens. Matter* **27**, 194127 (2015).
- [40] S. P. Pan, J. Y. Qin, W. M. Wang, and T. K. Gu, *Physical Review B* **84**, 092201 (2011).
- [41] S. Torquato and F. H. Stillinger, *Phys. Rev. E* **68**, 041113 (2003).
- [42] R. D. Batten, F. H. Stillinger, and S. Torquato, *J. Appl. Phys.* **104**, 033504 (2008).
- [43] P. K. Morse, J. Kim, P. J. Steinhardt, and S. Torquato, *Phys. Rev. Research* **5**, 033190 (2023).
- [44] M. Kac, G. E. Uhlenbeck, and P. C. Hemmer, *J. Math. Phys.* **4**, 216 (1963).
- [45] R. L. McGreevy, *J. Phys.: Condens. Matter* **13**, R877 (2001).
- [46] A. P. Thompson, H. M. Aktulga, R. Berger, D. S. Bolintineanu, W. M. Brown, P. S. Crozier, P. J. in 't Veld, A. Kohlmeyer, S. G. Moore, T. D. Nguyen, R. Shan, M. Stevens, J. Tranchida, C. Trott, and S. J. Plimpton, *Comput. Phys. Commun.* **271**, 108171 (2021).
- [47] J.-P. Hansen and I. McDonald, *Theory of simple liquids*, 3rd ed. (Academic Academic Press, 2006).
- [48] E. Lomba and J. L. López-Martín, *J. Stat. Phys.* **80**, 825 (1995).
- [49] G. Stell, *Journal of Statistical Physics* **78**, 197 (1995).
- [50] J. A. Bollinger and T. M. Truskett, *J Chem. Phys.* **145**, 064902 (2016).
- [51] G. Andrade, G. Ramos, D. Madeira, R. Sachetto, R. Ferreira, and L. Rocha, *Procedia Computer Science* **18**, 369 (2013).
- [52] B. G. Levine, J. E. Stone, and A. Kohlmeyer, *J. Comput. Phys.* **230**, 3556 (2011).
- [53] N. Sakharnykh, *GPU Pro Tip: Fast Histograms Using Shared Atomics on Maxwell*, Tech. Rep. (NVIDIA Corporation, 2015).
- [54] K. Reuter and J. Köfinger, *Computer Physics Communications* **236**, 274 (2019).
- [55] “IUPAC compendium of chemical terminology,” (2006) Chap. Radius of Gyration, 3rd ed.

- [56] F. Duang and J. Guojun, *Introduction to Condensed Matter Physics*, Vol. I (World Scientific, Singapore, 2005).
- [57] J.-P. Hansen and L. Verlet, *Phys. Rev.* **184**, 151 (1969).
- [58] S. Atkinson, G. Zhang, A. B. Hopkins, and S. Torquato, *Physical Review E* **94**, 012902 (2016).
- [59] D. Chen, E. Lomba, and S. Torquato, *Phys. Chem. Chem. Phys.* **20**, 17557 (2018).